

Enhanced dust emissivity power-law index along the western H α filament of NGC 1569

T. Suzuki^{1*}, H. Kaneda¹, T. Onaka², M. Yamagishi³, D. Ishihara¹, T. Kokusho¹ and T. Tsuchikawa¹

¹Graduate School of Science, Nagoya University, Furo-cho Chikusa-ku, Nagoya, 464–8602, Japan

²Department of Astronomy, Graduate School of Science, The University of Tokyo, 7-3-1 Hongo Bunkyo-ku, Tokyo, 113–0033, Japan

³Institute of Space and Astronautical Science, Japan Aerospace Exploration Agency, Sagamihara, Kanagawa 252–5210, Japan

16 March 2022

ABSTRACT

We used a data set from *AKARI* and *Herschel* images at wavelengths from 7 μm to 500 μm to catch the evidence of dust processing in galactic winds in NGC 1569. Images show a diffuse infrared (IR) emission extending from the galactic disk into the halo region. The most prominent filamentary structure seen in the diffuse IR emission is spatially in good agreement with the western H α filament (western arm). The spatial distribution of the F_{350}/F_{500} map shows high values in regions around the super-star clusters (SSCs) and towards the western arm, which are not found in the F_{250}/F_{350} map. The color-color diagram of F_{250}/F_{350} – F_{350}/F_{500} indicates high values of the emissivity power-law index (β_c) of the cold dust component in those regions. From a spectral decomposition analysis on a pixel-by-pixel basis, a β_c map shows values ranging from ~ 1 to ~ 2 over the whole galaxy. In particular, high β_c values of ~ 2 are only observed in the regions indicated by the color-color diagram. Since the average cold dust temperature in NGC 1569 is ~ 30 K, $\beta_c < 2.0$ in the far-IR and sub-mm region theoretically suggests emission from amorphous grains, while $\beta_c = 2.0$ suggests that from crystal grains. Given that the enhanced β_c regions are spatially confined by the HI ridge that is considered to be a birthplace of the SSCs, the spatial coincidences may indicate that dust grains around the SSCs are grains of relatively high crystallinity injected by massive stars originating from starburst activities and that those grains are blown away along the HI ridge and thus the western arm.

Key words: galaxies: dwarf – galaxies: halos – galaxies: ISM – galaxies: individual: NGC 1569 – infrared: galaxies.

1 INTRODUCTION

Understanding of galaxy evolution remains a key subject in modern astrophysics. Circulation of gas and dust on galactic scales has a large influence on the evolution of both the interstellar medium (ISM) and the intergalactic medium (IGM), and thus serves a vital role in galaxy evolution.

One of major drivers to eject the ISM into the IGM is galactic winds driven by mechanical energy and momentum from supernovae and stellar winds (e.g., Aguirre et al. 2001; Zu et al. 2011). Galactic winds are observationally found at all cosmic epochs and are very prominent and ubiquitous especially in the redshift range of $z \sim 2$ – 3 (Erb et al. 2012), which is the peak star formation period. The loss of gas from galaxies can quench their star-forming activities

and consequently can change the properties of the galaxies (e.g., Cazzoli et al. 2014). On the other hand, the presence of metal-enriched gas and dust grains in the IGM directly affects the thermal balance of gas. In particular, Montier & Giard (2004) show that infrared (IR) emission from dust grains can be considered as a dominant cooling agent of gas with temperatures of 10^6 – 10^8 K, which are the typical range in the IGM; the cooling efficiency by dust grains strongly depends on a dust-to-gas mass ratio (DGR) and a dust size distribution. The efficient cooling by dust grains induces an increase of star and dust formations, and may impact on hierarchical clustering of the large-scale structures. Despite the importance of the role of dust grains in galaxy evolutions, comprehensive understanding of the fate of dust due to galactic winds is not observationally established yet, although recent optical, IR and sub-millimeter (mm) observations of nearby starburst

* E-mail: t.suzuki@u.phys.nagoya-u.ac.jp

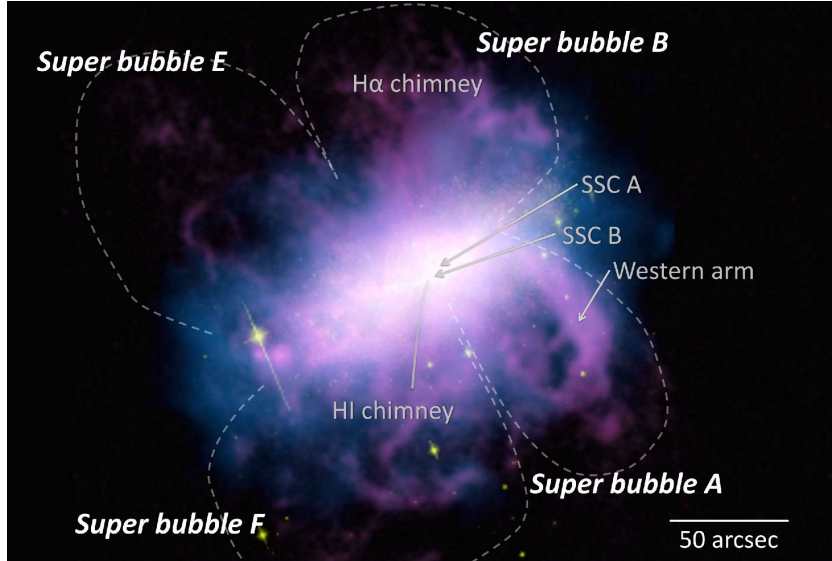


Figure 1. Composite image of NGC 1569: $0.66 \mu\text{m}$ ($\text{H}\alpha$) (magenta), $0.837 \mu\text{m}$ (green) and $70 \mu\text{m}$ (cyan). [Martin \(1998\)](#) defines the four-superbubble (A, B, E and F) regions denoted by the dashed line. $\text{H}\alpha$ filaments inside the superbubbles were identified by [Martin \(1998\)](#) and [Westmoquette et al. \(2008\)](#). The other features were identified by [Hodge \(1974\)](#), [Arp & Sandage \(1985\)](#), [Israel & van Driel \(1990\)](#), [Mühle et al. \(2005\)](#), and [Hunter et al. \(1993\)](#).

galaxies show extended emissions from dust grains and polycyclic aromatic hydrocarbons (PAHs) and revealed kinematics of PAHs in galactic winds (e.g., [Kaneda et al. 2010](#); [Roussel et al. 2010](#); [Yoshida et al. 2011](#)).

The dwarf-irregular galaxy NGC 1569 is an ideal laboratory to investigate dust processing in galactic winds and to insight into it in the early universe. Dwarf galaxies are believed to be the ‘building blocks’ of larger galaxies in the early universe. In particular, starburst dwarf irregular galaxies are expected to have experienced gravitational interactions or mergers. NGC 1569, a member of the IC 342 group of galaxies, may have interacted with a companion galaxy ([Johnson 2013](#)) and has undergone at least three major starburst phases; the most recent and strongest starburst ($\sim 3.2 M_{\odot} \text{yr}^{-1} \text{kpc}^{-2}$) started ~ 40 Myr ago and ended ~ 10 Myr ago ([Angeretti et al. 2005](#)). During this phase, the galaxy witnessed $\sim 10^4$ supernova explosions, and the formation of star clusters including the two prominent super-star clusters (SSCs) A and B ([Arp & Sandage 1985](#)). These activities have had dramatic effects on both the ISM and the halo of NGC 1569: (i) a cavity shown in the H I , $\text{H}\alpha$ and far-IR distributions centered on SSC A, most probably due to stellar winds from SSC A ([Israel & van Driel 1990](#); [Hunter et al. 2000](#); [Lianou et al. 2014](#)), (ii) chimneys in southward and northward directions from SSC A, which are considered to be major pathways to eject the ISM into the halo ([Hunter et al. 1993](#); [Mühle et al. 2005](#); [Westmoquette et al. 2008](#)), (iii) a bipolar metal-enriched outflow comprising kpc-scale expanding superbubbles on the southern and northern sides of the galactic disc ([Hunter et al. 1993](#); [Heckman et al. 1995](#); [Martin 1998](#); [Martin et al. 2002](#); [Westmoquette et al. 2008](#)).

As shown in Fig. 1, $\text{H}\alpha$ observations show that the halo contains four expanding superbubbles (A, B, E and F; [Martin 1998](#)), which include a number of cellular filaments excited by shocks; their dynamical ages are roughly esti-

ated to be 10–25 Myr from their expanding velocities ($80\text{--}100 \text{ km s}^{-1}$) and diameters ($\sim 1 \text{ kpc}$) ([Westmoquette et al. 2008](#)). The ages are consistent with the starburst histories of SSC A and B ([Angeretti et al. 2005](#)). It indicates that each superbubble is associated with a star-forming event. [Martin et al. \(2002\)](#) found the two-component diffuse X-ray emissions in the halo region; the softer and brighter X-ray component ($0.3\text{--}0.7 \text{ keV}$) is found adjacent to the $\text{H}\alpha$ filaments, while the harder X-ray component ($0.7\text{--}1.1 \text{ keV}$) is likely spatially correlated with the centers of the superbubbles. The softer and brighter X-ray component is associated with shocks caused by galactic wind-halo interactions.

At a position in the most prominent $\text{H}\alpha$ filament (western arm), [Onaka et al. \(2010\)](#) found the presence of the unidentified infrared (UIR) bands at 3.3 , 6.2 , 7.7 and $11.3 \mu\text{m}$ by *AKARI*/*IRC* spectroscopic observations. Under the shock environment, the destruction timescale ($\sim 10^3 \text{ yr}$) of the UIR band carriers, which have been possibly attributed to PAHs, is much shorter than the dynamical timescales of the galactic wind in superbubble A (cf. [Micelotta et al. 2010](#)). The result may indicate that the band carriers are produced by fragmentation of larger grains in shocks and that dust processing took place over a wide area of the halo region. Despite the possibility, extensive investigations on dust processing in galactic winds from NGC 1569 have never been reported because of a lack of spatially resolved far-IR images before the *Herschel* era.

In this paper, using a data set from *AKARI* ([Murakami et al. 2007](#)) and *Herschel* ([Pilbratt et al. 2010](#)) imaging observations at wavelengths from $7 \mu\text{m}$ to $500 \mu\text{m}$, we report spatial distributions of dust grains entrained by galactic winds from NGC 1569 based on pixel-by-pixel spectral energy distribution (SED) fitting to catch the evidence of dust processing in galactic winds.

Table 1. Summary of the IR and sub-mm imaging data set taken from the *AKARI* and *Herschel* data archives.

Telescope/Instrument	λ (μm)	FWHM ($''$)	Observation IDs	$1-\sigma$ background noise (MJy sr^{-1})
<i>AKARI</i> /IRC	7	5.1	1400423	3.4×10^{-2}
<i>AKARI</i> /IRC	11	4.8	1400423	4.5×10^{-2}
<i>AKARI</i> /IRC	15	5.7	1400424	4.2×10^{-2}
<i>AKARI</i> /IRC	24	6.8	1400424	1.2×10^{-1}
<i>Herschel</i> /PACS	70	5.6	1342243816–1342243821	1.0
<i>Herschel</i> /PACS	160	11.4	1342243816–1342243821	1.6
<i>Herschel</i> /SPIRE	250	18.4	1342193013	1.3
<i>Herschel</i> /SPIRE	350	25.2	1342193013	1.5
<i>Herschel</i> /SPIRE	500	36.7	1342193013	0.4

2 OBSERVATIONS AND DATA ANALYSIS

NGC 1569 was observed as part of the *AKARI* mission program ‘ISM in our Galaxy and Nearby Galaxies’ (ISMGN – P.I. Kaneda H.; Kaneda et al. 2009a) and as part of the *Herschel* programs ‘the Dwarf Galaxy Survey’ (DGS – P.I. Madden S.; Madden et al. 2013) and ‘Exploring the Dust Content of Galactic Winds with *Herschel*: The Dwarf Galaxy Population’ (PI: Veilleux S.). We used *AKARI*/IRC (Onaka et al. 2007) and *Herschel*/PACS-SPIRE imaging data (Poglitsch et al. 2010; Griffin et al. 2010), which were taken from data archives: the *AKARI* pointing data archive through the data archive and transmission system (DARTS) and the *Herschel* Science Archive (HSA). Table 1 lists the summary of the data used in this study.

The IRC data obtained with the IRC02 observation mode provide mid-IR images with four bands (7, 11, 15 and 24 μm), which are finely allocated for probing emission from PAHs and very small grains. Each field-of-view has a size of about $10' \times 10'$. The details of the observations are described in Onaka et al. (2010); the FWHM of the point spread function (PSF) ranges from $\sim 5''$ to $\sim 7''$. The mid-IR images with a pixel size of $2''3$ were created by using the IRC imaging pipeline software version 20131202; overall four-band images thus obtained are the same as those shown in Fig. 1 of Onaka et al. (2010). However, for the four-band mid-IR images, in particular the IRC 24 μm image, mid-IR emission in the halo region of interest is affected by an extended component of the PSF due to diffraction and scattering when bright sources such as SSCs are observed. To correct for the extended PSF effects, the image reconstruction method proposed by Arimatsu et al. (2011) was applied for the four-band images; the method consists of the deconvolution with the intrinsic PSF of an input image and of the convolution with a Gaussian pattern with the same FWHM of the PSF. To apply the convolution, the pixel size of the four-band images was reduced by a factor of 2 ($1''15$). Furthermore, the point sources located in the halo region were removed with the following procedures: first, a point source was fitted with a model of 2-D gaussian plus constant components so that the gaussian center is located at the peak brightness of the point source. The radius of each fitting area is set to be three times as large as the FWHM. Second, the gaussian component was subtracted from the original image. Finally, for subtracted pixels, values below the mean

surface brightness given by the constant component were replaced by the mean surface brightness. A series of procedures was applied to each point source. The systematic flux uncertainty, which is dominantly caused by the PSF reconstruction, is estimated to be 7.4% (IRC 7 μm), 7.5% (IRC 11 μm), 18% (IRC 15 μm) and 16% (IRC 24 μm).

Cross-linked observations were performed by the PACS, and simultaneously provide 70 and 160 μm -band images which cover an area of $\sim 7' \times 9'$ around NGC 1569. Both data were taken from the HSA and are level-3 products (SPG version 14.2.0) providing Unimap maps. The FWHM of the PSF is $5''6$ for PACS 70 μm and $11''4$ for PACS 160 μm . The systematic flux calibration uncertainty is 5% for both bands (PACS Observer’s Manual version 2.5.1, 2013).

SPIRE large cross-scan observations provide 250, 350 and 500 μm -band images at the same time and cover an area of $\sim 20' \times 20'$ around NGC 1569 in each band. The details of the observations are described in Rémy-Ruyer et al. (2013). The SPIRE data were taken from the HSA and are level-2 products (SPG version 14.1.0) providing *Naive* maps with the pixel sizes of $6''$ for SPIRE 250 μm , $10''$ for SPIRE 350 μm and $14''$ for SPIRE 500 μm . The beam size has the FWHMs of $18''4$, $25''2$ and $36''7$ at SPIRE 250 μm , SPIRE 350 μm and SPIRE 500 μm , respectively. The systematic flux calibration uncertainty of the three SPIRE bands is applied to be $\sim 5\%$ (SPIRE Observer’s Manual version 2.5, 2014).

A background level was estimated by averaging the values from multiple apertures placed around $2' - 3'$ away from the galaxy center without overlapping with extended emission and was subtracted from each image. For multi-band analysis, the spatial resolutions of background-subtracted IR images were reduced to match the PSF of the SPIRE 500 μm data by convolving PACS and SPIRE-band images with kernels provided by Aniano et al. (2011). Because such kernels for the *AKARI* bands are currently not available in the library¹, the *AKARI* images were convolved by a Gaussian kernel to approximate the SPIRE 500 μm PSF by the *moderate* Gaussian FWHM of $41''$ (Aniano et al. 2011). Then, the convolved images were regridded with a pixel size of $36''7$ matched with the PSF of the SPIRE 500 μm data.

¹ <http://www.astro.princeton.edu/~ganiano/Kernels.html>

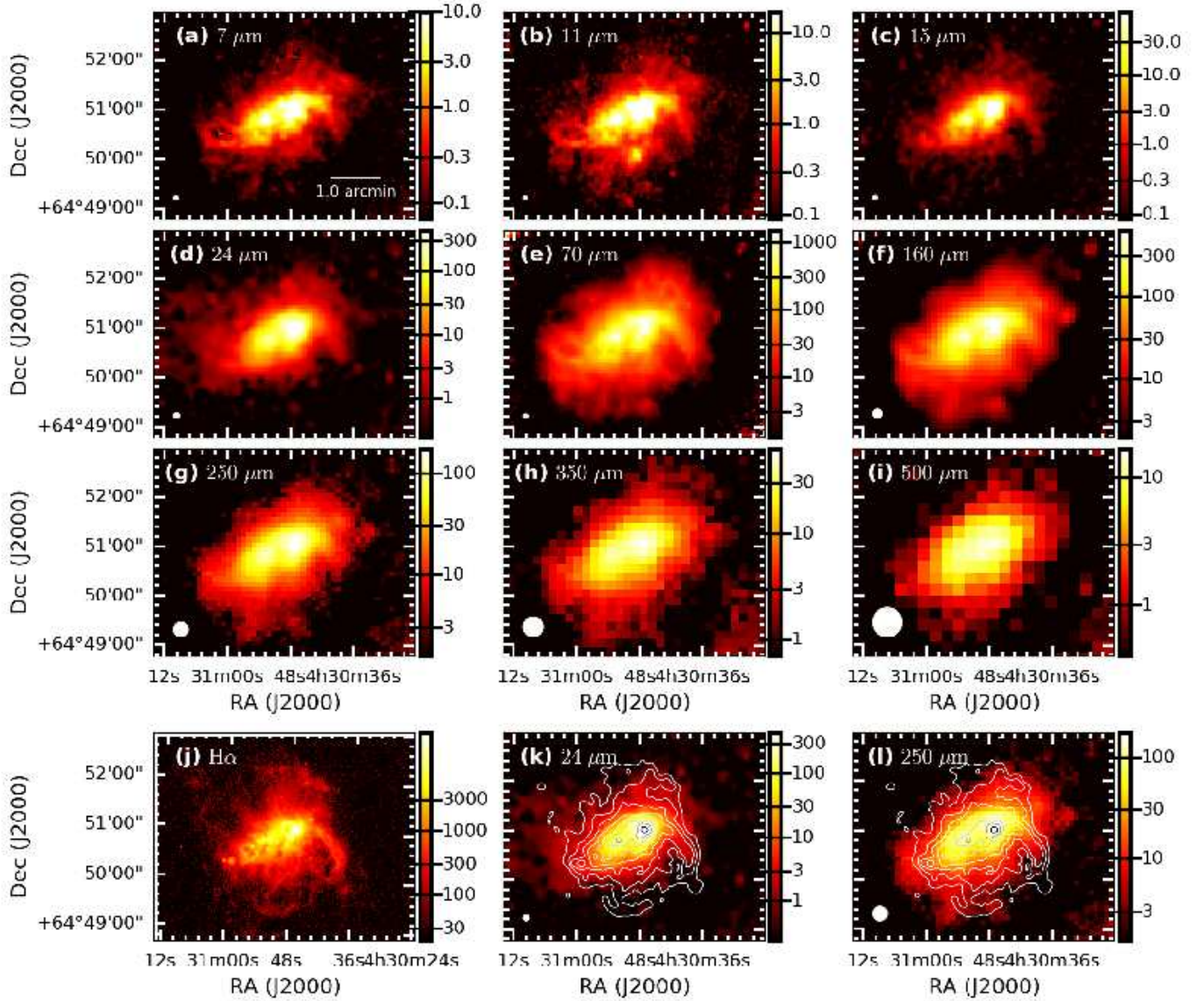


Figure 2. Background-subtracted nine-band images of NGC 1569 with the *AKARI*/IRC and *Herschel*/PACS-SPIRE in the (a) IRC 7 μm , (b) IRC 11 μm , (c) IRC 15 μm , (d) IRC 24 μm , (e) PACS 70 μm , (f) PACS 160 μm , (g) SPIRE 250 μm , (h) SPIRE 350 μm and (i) SPIRE 500 μm bands. In each image, the color bar is given in units of MJy sr^{-1} . The PSF size in FWHM is shown in the lower left-hand corner. For comparison with the spatial distribution of the $\text{H}\alpha$ emission shown in the panel (j) (Hunter & Elmegreen 2004), the same panels of (d) and (g) are shown together with the $\text{H}\alpha$ contours in panels (k) and (l).

3 RESULTS

3.1 IR images

Figure 2 shows the background-subtracted images of NGC 1569 obtained with *AKARI* and *Herschel*. To compare them with the spatial distribution of the $\text{H}\alpha$ emission shown in the panel (j) (Hunter & Elmegreen 2004), the same panels of (d) and (g) are shown together with the $\text{H}\alpha$ contours in panels (k) and (l). The $1-\sigma$ background fluctuations per pixel are $0.04\text{--}0.1 \text{ MJy sr}^{-1}$ for $7\text{--}24 \mu\text{m}$ and $0.4\text{--}1.6 \text{ MJy sr}^{-1}$ for $70\text{--}500 \mu\text{m}$ (Table 1). Most of the images clearly show diffuse IR emission extending from the galactic disk into the halo region (hereafter referred to as IR-halo emission). Filamentary structures seen in the $\text{H}\alpha$ emission are spatially

correlated with those seen in the IR-halo emission. In superbubbles A and E, a pair of filaments which outline the western and eastern sides of each superbubble is observed in mid-IR to sub-mm images; the most prominent IR filament is spatially in good agreement with the western arm. In superbubble B, the IR-halo emission extends toward north along the $\text{H}\alpha$ chimney. With regard to superbubble F, which is formed by the ISM escaping from the galactic disk through the H I chimney (Westmoquette et al. 2008), patchy IR-halo emission is observed along $\text{H}\alpha$ filaments. Furthermore, the IR-halo emission also shows the component extending in the major-axis direction over the $\text{H}\alpha$ emission.

The IRC 7 μm and 11 μm images are dominated by the PAH emission not only from the galactic disk itself but

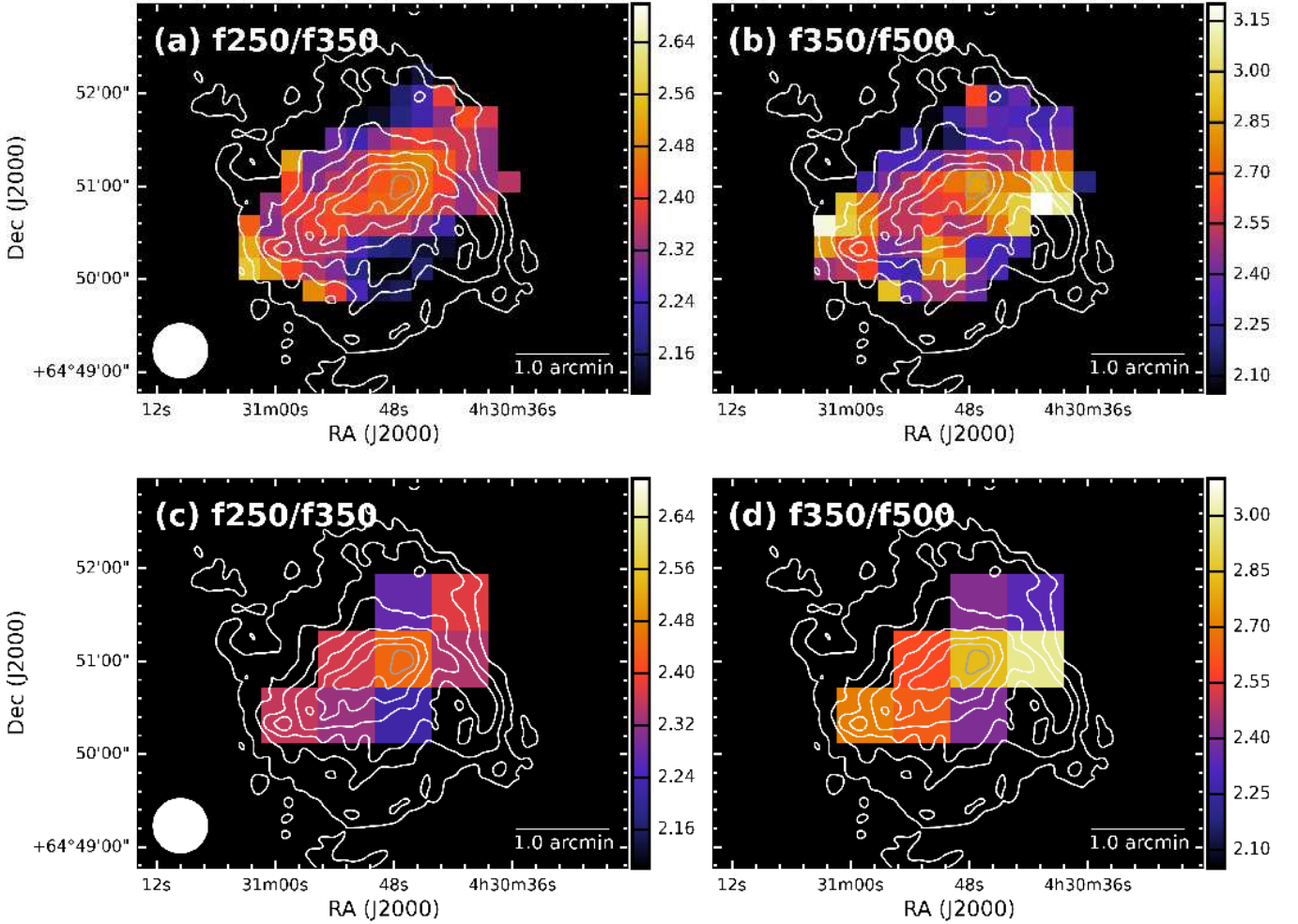


Figure 3. Color maps of (a) F_{250}/F_{350} , and (b) F_{350}/F_{500} with the original pixel size of the SPIRE 500 μm data ($14''$). Panels (c) and (d) are the same as (a) and (b), but with a pixel size of $36''$, respectively. The PSF shown in the panels (a) and (c) is matched to the SPIRE 500 μm -band PSF. The detection threshold is set to be the 5σ level for each band image. The contours superimposed on the images are the same as those in Fig. 2.

also from the halo; Onaka et al. (2010) detected the PAH emission from the western arm. Overall spatial distributions in the 7 μm and 11 μm images are in good agreement with those in the 160–500 μm images which trace the spatial distribution of the cold dust component (20–30 K, Rémy-Ruyer et al. 2013; Lianou et al. 2014), associated mainly with the old stellar population. The fact may indicate that PAHs coexist with cold dust. The IRC 15 μm and 24 μm images trace emission from both hot (100–200 K) and warm (40–60 K) dust components (Lianou et al. 2014; Galliano et al. 2003), associated mainly with massive star-forming regions. Therefore, the spatial distributions of cold and PAH components are more extended toward the halo region than those of hot and warm dust components.

3.2 Color-color diagram: F_{250}/F_{350} – F_{350}/F_{500}

To obtain a global view of the variation in the shape of the cold dust component in the local SEDs, sub-mm colors are a simple and useful quantitative tool to avoid potential con-

tamination from the warm dust component (Bendo et al. 2012, 2015). As demonstrated by Boselli et al. (2012), we created F_{250}/F_{350} and F_{350}/F_{500} color maps. The errors on the flux densities (σ) were calculated from $(\sigma_{\text{sys}}^2 + \sigma_{\text{stat}}^2)^{1/2}$, where σ_{sys} and σ_{stat} are systematic and statistical uncertainties, respectively.

In Figs. 3a and 3b that were regridded with the original pixel size of the SPIRE 500 μm data ($14''$) for a display purpose, values of the F_{250}/F_{350} show almost constant over the whole region, while F_{350}/F_{500} values are higher in the southern halo region, in particular the western arm, than in the northern halo region. Those trends can clearly be confirmed in the sub-mm color-color diagram. The filled circles in Fig. 4 represent the observed color-color diagram at each pixel of the F_{250}/F_{350} and F_{350}/F_{500} maps (Figs. 3c and 3d). The solid lines are the model-predicted color-color diagram based on a single-component modified blackbody model with the emissivity power-law index (hereafter referred to as the emissivity index) of 1.0 (leftmost line), 1.5, 2.0, and 2.5 (rightmost line). The constant temperature points are connected

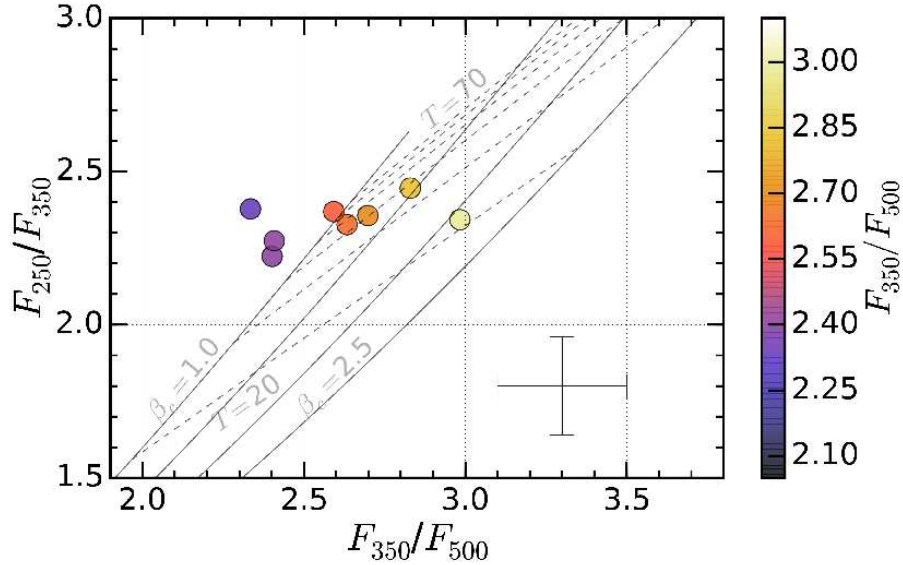


Figure 4. F_{250}/F_{350} – F_{350}/F_{500} diagram. The filled circle represents the observed color-color diagram at each pixel shown in Figs. 3c and 3d, while the solid lines are the color-color diagram based on a single-component modified blackbody model defined as $\nu^{\beta_c} B_\nu(T_c)$ for $\beta_c=1.0$ – 2.5 with a step of 0.5 . The color of each data point is the same as that of each pixel in Fig. 3d. The constant temperature points are connected by the dashed lines for temperatures from 20 (bottom line) to 70 K (top line) with a step of 10 K. A typical error bar is shown in the lower right corner.

by the dashed lines for temperatures from 20 K (bottom line) to 70 K (top line) with a step of 10 K. The color-color diagram suggests that the plots in and around the disk region tend to distribute along the direction of the temperature change with $\beta \sim 1$, while those in the IR-halo region tend to distribute relatively along the constant temperature lines (dashed lines) rather than the constant β lines; the western arm region shows higher β (~ 2), while the northern halo region of the SSCs shows lower β ($\lesssim 1$). Since it is possible that color values are affected by noise as a limitation of the color-color analysis, further confirmation of the β variation is required by performing SED fitting.

3.3 Spectral decomposition into cold dust, warm dust and PAH components

Spectral decomposition analysis on a pixel-by-pixel basis provides investigations on the spatial distributions of dust properties such as dust temperature and emissivity index. An individual SED constructed from the nine-band fluxes at each pixel is reproduced by a double-component modified blackbody plus a PAH model expressed as

$$F_{V,IR} = A_{PAH} F_{V,PAH} + A_c \nu^{\beta_c} B_\nu(T_c) + A_w \nu^{\beta_w} B_\nu(T_w) \left\{ 1 + \left(\frac{\nu_c}{\nu} \right)^\alpha e^{-\left(\frac{\nu_c}{\nu} \right)^2} \right\}, \quad (1)$$

where T_c , T_w , β_c , β_w , A_c , A_w , A_{PAH} , and $B_\nu(T)$ are the temperatures of cold and warm dust, the dust emissivity indices of cold and warm dust, the amplitudes of cold dust, warm dust, PAH components, and the Planck function, respectively. The second term in the warm dust component is the analytic approximation of dust emission with different dust temperatures assuming a power-law tempera-

ture distribution to take the hot dust component into account in mid-IR wavelengths (Casey 2012). The power-law turnover frequency ν_c defined by Casey (2012) is a function of the mid-IR power-law slope α and T_w . The flux density of the PAH component, $F_{PAH}(\nu)$, is calculated as described in Suzuki et al. (2010) and is based on the PAH parameters taken from Li & Draine (2001) and Draine & Li (2007) by assuming the PAH size distribution ranging from 3.55 to 300 Å, the fractional ionization and the temperature probability distribution for the typical diffuse ISM with the interstellar radiation field in the solar neighborhood. PAHs with sizes larger than 15 Å contribute to ~ 20 μm continuum emission (Draine & Li 2007). Since very small grains (VSGs) which are stochastically heated by absorbed photons contribute to ~ 20 μm continuum emission, the PAH component in Eq. (1) takes the VSG emission into account.

3.3.1 Pixel-by-pixel SED fitting

Since Fig. 4 indicates the β_c variation over the disk-IR halo region, β_c is set to be free, while β_w is assumed to be constant over the disk-IR halo region. To confirm that the assumption does not affect the result of the β_c variation, we performed pixel-by-pixel SED fitting for each of $\beta_w=1.0$, and 2.0 . In general, when T_d and β are treated as fitting parameters, a β – T_d anti-correlation is expected (Tabatabaei et al. 2014, and references therein). The anti-correlation mainly comes from β – T_d degeneracy; for a set of data points, a high goodness of fit can be obtained for different (β , T_d) pairs. To avoid the artificial anti-correlation, one fitting cycle consists of the following two steps: the first fitting step with fixed T_c and free β_c , and second fitting step with free T_c and fixed β_c . A series of fitting cycles for each pixel was performed and was

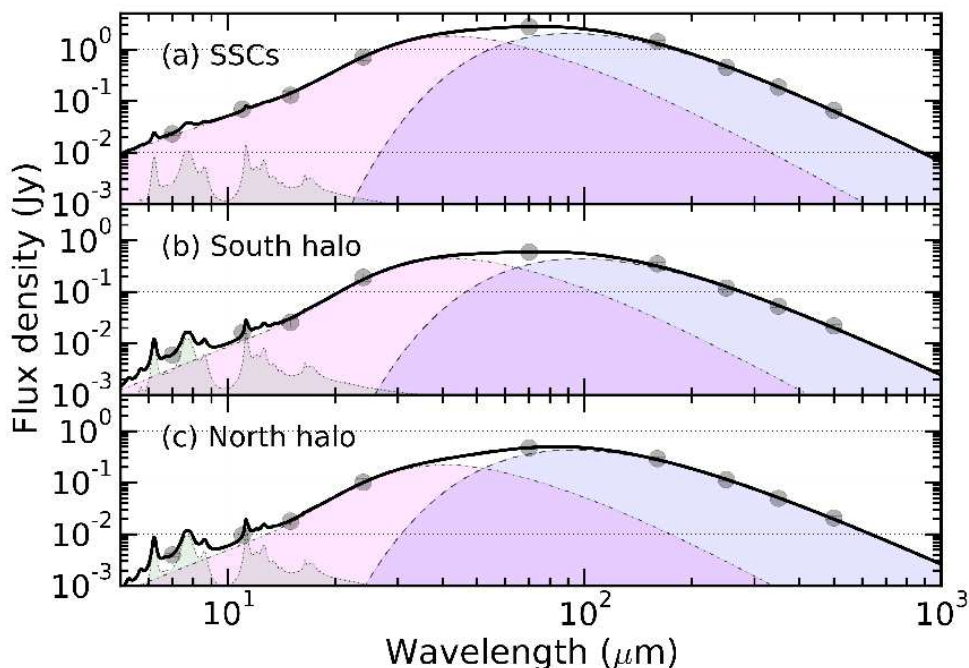


Figure 5. SEDs at pixel ($36''7$) positions of (a) SSCs, (b) south halo, and (c) north halo regions as denoted by open circles in Fig. 6a. At each panel, the solid thick line shows the best-fit model with $\beta_w = 2.0$, which is described in Eq. (1). The cold dust, warm dust, and PAH components are indicated by dashed, dash-dotted, and dotted lines, respectively. The PSF is matched to the SPIRE 500 μm -band PSF.

completed when χ^2 converges with the lowest value. Thus, at each pixel, the six-free parameters (T_c or β_c , T_w , A_c , A_w , A_{PAH} , and α) are derived from the nine bands.

To minimize the probability of falling into local minima of the merit function, $\Sigma(F_{\text{model}} - F_{\text{obs}})^2/\sigma^2$, where σ is the flux uncertainty, we generated uniform samples of 10^6 random sets of the six parameters. As for each parameter, the random value ranges within 5% from the input value which is obtained from the previous fitting step. For the first fitting cycle, input values of T_c and T_w were set to be the values obtained from SED fitting of the whole galaxy with $\beta_c = 1.5$ and $\beta_w = 1.0$ or 2.0. From each random set of the six parameters, $F_{\text{V,IR}}$ at each wavelength was calculated. For each pixel, the initial parameter set which provides the fluxes most closest to those observed was chosen by maximizing the likelihood. Then, using the initial parameter set, pixel-by-pixel SED fitting was performed to minimize χ^2 . Color corrections to the IRC 15 μm , 24 μm , PACS and SPIRE-band fluxes were iteratively performed with the assumption of a modified blackbody spectrum for each fitting cycle. As a result, the six parameters with $\beta_w = 2.0$ better reproduce the observed fluxes with pixel-averaged χ^2_{ν} ($d.o.f = 3$) of 0.6. Figure 5 shows SEDs at pixel positions of (a) SSCs, (b) south halo, and (c) north halo regions, which are denoted by open circles in Fig. 6a, together with the best-fit model.

3.3.2 Spatial distributions of β_c , T_c , and T_w

Figure 6 shows the spatial distributions of β_c (top), T_c (middle), and T_w (bottom). The panels in the left and right

columns show their maps obtained with β_w of 1.0, and 2.0, respectively. Moreover, Fig. 7 shows the maps with a higher spatial resolution obtained from SED fitting using the eight-band images (IRC 7 μm –SPIRE 350 μm), whose PSFs were matched to the SPIRE 350 μm -band PSF. Uncertainties in β_c , T_c , and T_w are 4%, 5%, and 6%, respectively. From Figs. 6 and 7, it is confirmed that overall spatial distributions of β_c , T_c , and T_w are independent of the β_w values.

As suggested by the color-color diagram, Fig. 6 shows that high β_c values are observed around the western arm and SSCs regions. In fact, the pixel-by-pixel comparison of β_c in Fig. 8 shows that the β_c values obtained from SED fitting (β_{SED}) are in agreement with those from the F_{350}/F_{500} color (β_{color}), which are obtained with a single-component modified blackbody model. The result suggests that β_{SED} is not influenced by the warm dust component. The β_c map with a higher spatial resolution (25''2, Fig. 7) reveals that β_c shows almost constant value of ~ 1.5 in the disk region, but high β_c values as high as ~ 2 are found around the SSCs and in regions towards the western arm. As for the IR-halo region, enhanced β_c values (~ 2) are clearly observed along the western arm in superbubble A, while such high β_c values are not observed in other three superbubbles; the lowest β_c values are observed in superbubble B.

The T_w map in Fig. 7 is in agreement with the $H\alpha$ map in the disk region. High- T_w values are observed near current star-forming regions such as the SSCs, while the T_c map shows a more uniform distribution than the T_w map; high- T_c values are found around SSCs. Those results are consistent with the spatial distribution of T_c shown in Lianou et al. (2014). In the IR-halo region, both T_c and T_w are found to

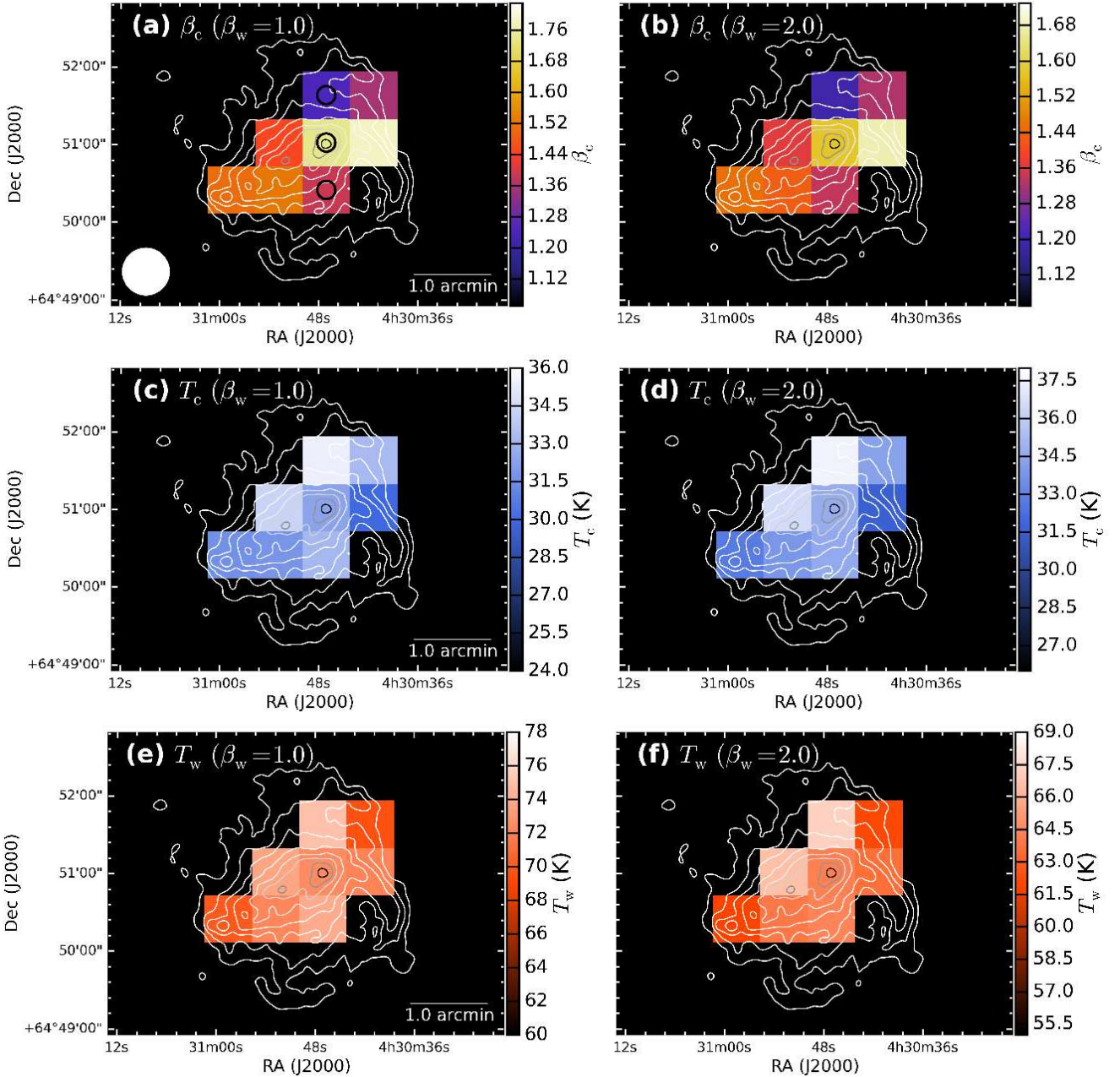


Figure 6. Spatial distributions of β_c (top), T_c (middle), and T_w (bottom). In each column, left and right panels show their maps with $\beta_w = 1.0$ and 2.0, respectively. The open circles in the panel (a) represent pixel positions of SEDs in SSCs, south halo, and north halo regions (see Fig. 5). The detection threshold is set to be the 5σ level for each band image. The contours superimposed on the images are the same as those in Fig. 2. The PSF size in SPIRE $500 \mu\text{m}$ is shown in the lower left-hand corner on the panel (a). The pixel size is the same as the original one of the SPIRE $500 \mu\text{m}$ data ($36''7$).

be systematically higher on the northern side than on the southern side. Those high-temperature dust grains tend to be spatially matched adjacent to the $H\alpha$ filaments of superbubbles B and E.

Figure 9 shows the β_c – T_d relation obtained from Figs. 6b and 6d (filled square) and from individual dwarf galaxies observed by Herschel (Rémy-Ruyer et al. 2013, 2015). Although Rémy-Ruyer et al. (2013) investigated β and T_d values for the dwarf galaxy samples, they used the data sets processed with an older calibration version than our version. Thus, we reanalyzed β and T_d values for the samples us-

ing flux densities shown in Rémy-Ruyer et al. (2015), which were calibrated with the latest version, by applying the same SED fitting procedure as described in Rémy-Ruyer et al. (2013). The distribution of our data points overlaps well with the β – T_d anti-correlation from individual dwarf galaxies observed by Herschel (Rémy-Ruyer et al. 2013, 2015). Furthermore, our data plots are in agreement with that for the whole galaxy of NGC 1569 (black-filled circle).

To check if the observed β_c – T_d relation comes from the artificial anti-correlation, we compared input ($\beta_{c,\text{in}}, T_{c,\text{in}}$) with output sets of ($\beta_{c,\text{out}}, T_{c,\text{out}}$) by SED fitting of the mock

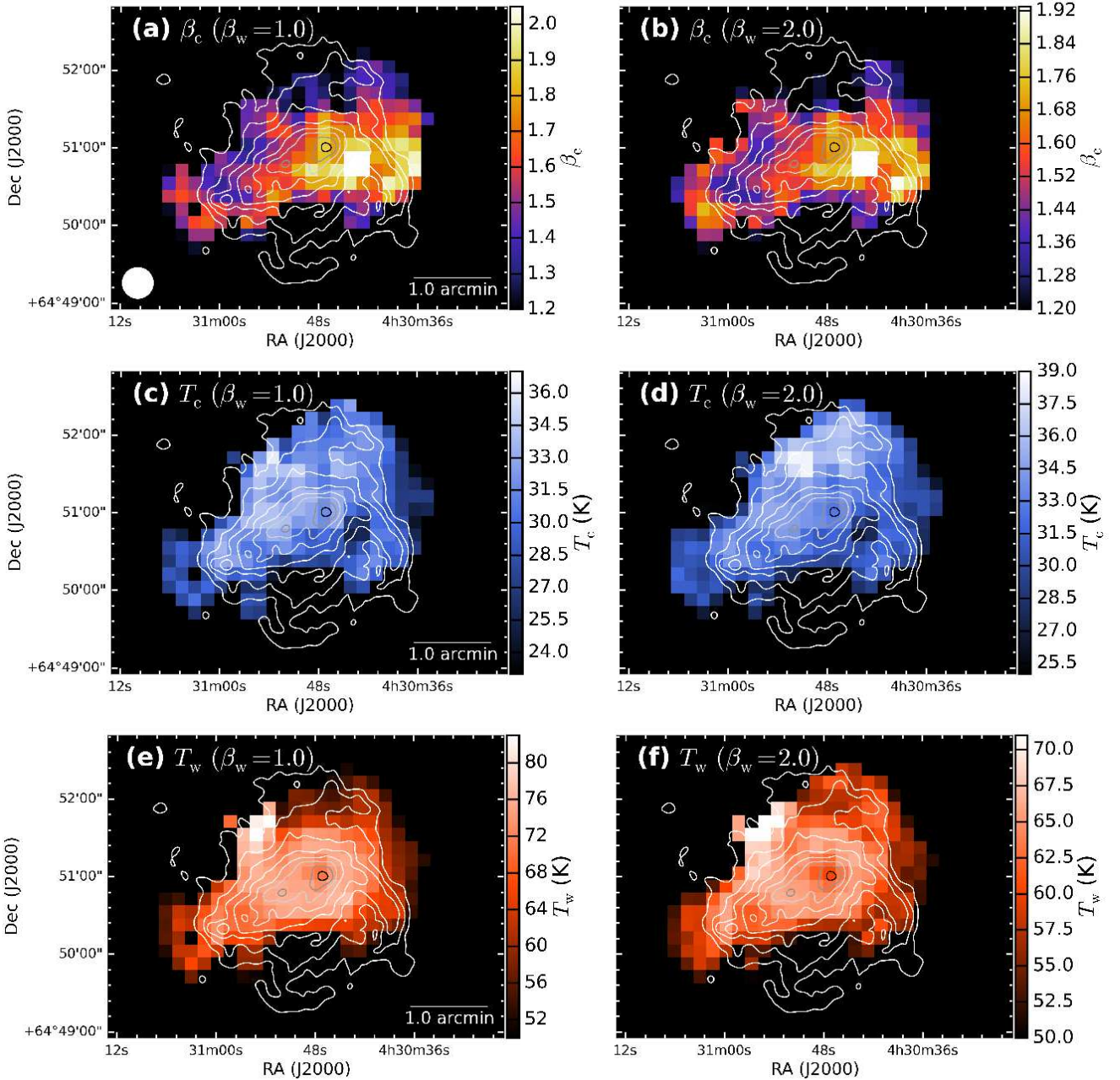


Figure 7. Same as Fig. 6, but the maps obtained from SED fitting using the eight-band images (IRC 7 μm –SPIRE 350 μm) to show the maps with a higher spatial resolution matched to the SPIRE 350 μm -band PSF ($25''.2$). The pixel size is the same as the original one of the SPIRE 350 μm data ($10''$).

data sets. We generated uniform samples of 2000 random sets of the seven-SED parameters; each parameter value is uniformly distributed within the range of 5% of the original best-fit parameter value to construct realistic mock SEDs. Then, each random set of the seven-SED parameters is used to synthesize flux densities for $\beta_w = 2.0$ given by Eq. (1) at each wavelength. Finally, the same SED fitting procedure as described in Sect. 3.3.1 was applied to the mock data sets. Figure 10 shows output/input ratio of β_c and T_c after taking average in each β_c bin (10 bins for the β_c range of 1.0–2.0). In this figure, although the artificial anti-correlation is confirmed, the range of both β_c and T_c variations is within $\sim 3\%$. Therefore, the observed β_c – T_d relation is not signifi-

cantly influenced by the artificial anti-correlation. Moreover, the enhanced β_c values reflect variations in the shape of the cold dust component in observed SEDs.

4 DISCUSSIONS

4.1 Enhanced β_c values along the western arm

H α observations reveal a number of filaments excited by shocks, which are associated with the four expanding superbubbles (Westmoquette et al. 2008). Moreover, the superbubbles are filled both with dust grains (see Fig. 2) and hot plasma (Martin et al. 2002). Among those H α filaments,

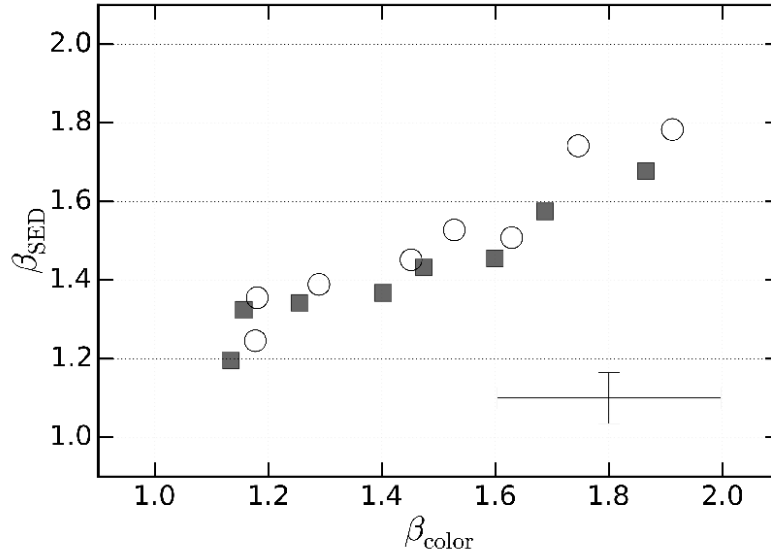


Figure 8. Relation between β_c from the F_{350}/F_{500} color (β_{color}) and β_c from the SED fitting (β_{SED}) with $\beta_w = 1.0$ (circle) and 2.0 (square) cases. The β_c values are obtained based on the SPIRE 500 μm -band PSF with a pixel size of $36''7$. A typical error bar is shown in the lower right corner.

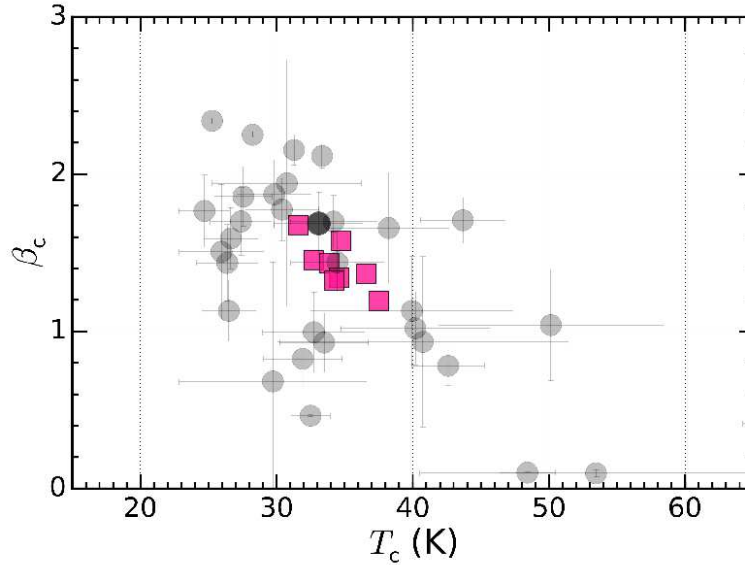


Figure 9. Pixel-by-pixel based β_c - T_c relation (filled square) overplotted on the relation for individual dwarf galaxies from the Dwarf Galaxy Survey with *Herschel* (filled circles). The filled square is obtained from Figs. 6(b) and (d) with the SPIRE 500 μm -band PSF. $\beta_c \gtrsim 1.7$ is found in the western arm. The black-filled circle denotes the plot for the whole region of NGC 1569.

dust grains associated with the western arm clearly show enhanced β_c values. Why are such grains observed along the western arm only?

Theoretically, the Lorentz model gives $\beta=2.0$ in far-IR and sub-mm region for perfect ionic crystal grains such as crystalline silicate dust. [Meny et al. \(2007\)](#) proposed a model for dust emission in far-IR and sub-mm region based on physical properties of amorphous material (e.g., amorphous silicate). They introduced a disordered charge distribution combined with the presence of two level tunneling

states to explain a wavelength and temperature-dependent β . The model with standard parameters well reproduced Galactic dust emission that mainly comes from amorphous silicate grains ([Paradis et al. 2011](#)); the model with the parameters predicts $\beta < 2.0$ for the dust temperature of ~ 30 K, which is the average T_c in NGC 1569.

The fact that $\beta_c \sim 2$ is continuously observed from the region around the SSCs to the western arm may attribute to starburst activities in the SSCs. Figure 11 shows the β_c map together with HI integrated contours ([Walter et al.](#)

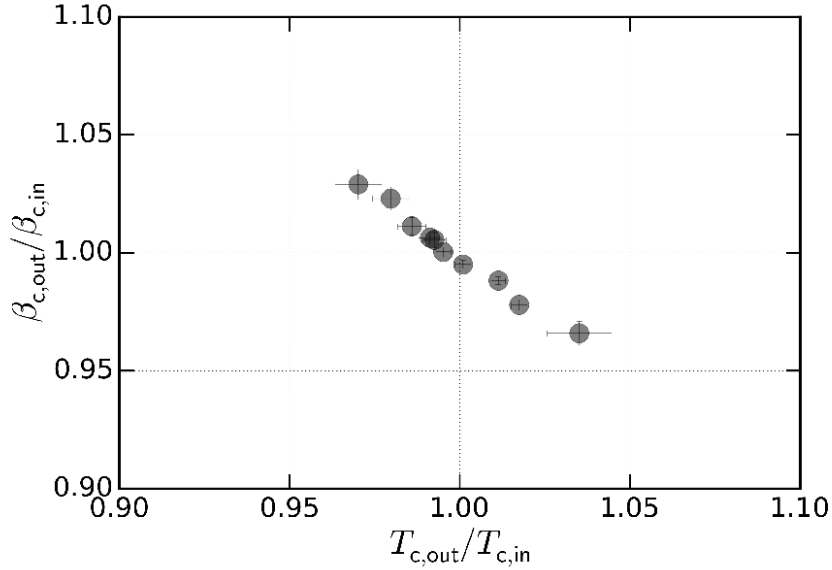


Figure 10. Output/input ratio of β_c and T_c based on SED fitting of the mock data sets with $\beta_w = 2.0$. Each filled circle shows the average of $(\beta_{c,out}/\beta_{c,in}, T_{c,out}/T_{c,in})$ sets in each β_c bin: 10 bins for the β_c range of 1.0–2.0.

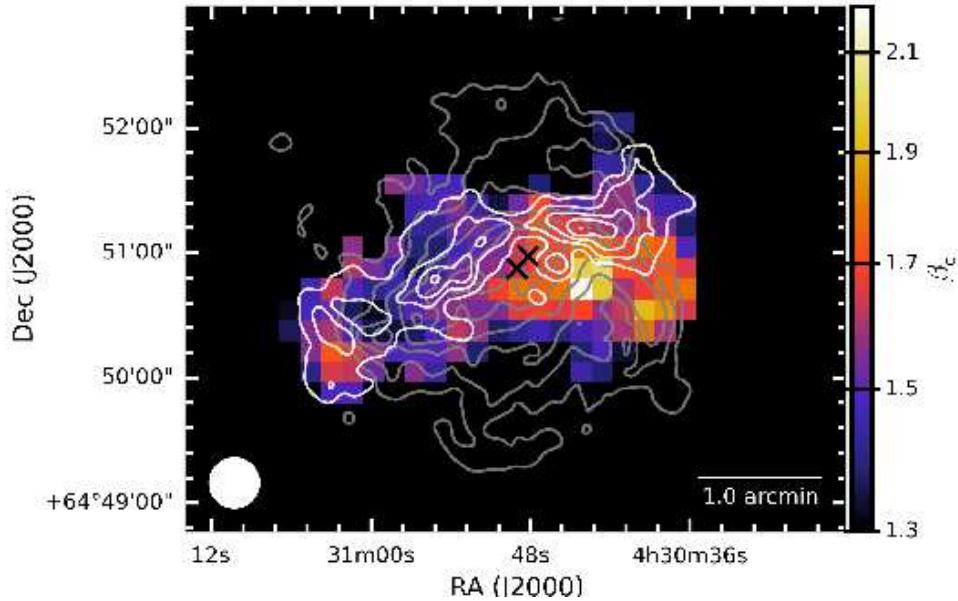


Figure 11. Same as Fig. 7b but different color scale to show regions with $\beta_c \sim 2$. The white contours superposed on the image show the integrated HI (Walter et al. 2008), while the gray contours are the same as those in Fig. 2. Two cross marks are the positions of SSC-A (right) and B (left).

2008). In the disk, the values of $\beta_c \sim 2$ are distributed around the SSCs (two cross marks), and the region is clearly confined by two dense HI clouds called as the HI ridge (Israel & van Driel 1990; Mühle et al. 2005). Given that the SSCs are located in between these two dense HI clouds, as pointed out by Johnson et al. (2012), the SSCs are likely to be formed out of the HI ridge that used to connect these two dense HI clouds. Those spatial coincidences may indicate that dust grains around the SSCs are crystalline ones produced by massive stars originating from starburst activities as have been found in ultra-luminous in-

frared galaxies (Spoon et al. 2006), since the latest starburst phase ended 5–10 Myr ago (Angeretti et al. 2005), which is shorter than the crystalline-to-amorphous conversion timescale of 40–70 Myr due to cosmic-ray hits (Spoon et al. 2006; Kemper et al. 2011). This might indicate that crystalline grains injected by massive stars are blown away along the HI ridge and thus the western arm.

4.2 Origins of dust heating in the IR-halo region

In the IR-halo region, spatial distributions of T_c and T_w are asymmetric with respect to the disk. Two possible heating sources are considered. One is radiative heating by stars distributed over the disk. In this case, the observed dust temperatures should monotonically decrease away from the disk. Therefore, the observed dust temperatures and their distributions in the IR-halo region cannot be explained solely by radiative dust heating. This means that an additional heating source is required.

The other heating source is collisional heating mainly with electrons in a hot plasma; the possibility is also pointed out for dust heating in the halo region of NGC 253 by Kaneda et al. (2009b). Dwek (1987) presented a detailed analysis of collisional heating of dust grains under various plasma conditions with temperatures above $\sim 10^6$ K. According to Dwek (1987), dust temperatures due to collisional heating were calculated by taking the following conditions into account; for the calculation of the collisional heating rate of dust grains, a collision partner is mainly electrons. As for the cooling rate of dust grains, the dust absorption coefficient is applied for silicate and carbonaceous grains with their sizes of 0.01–1.0 μm . Since the average number density and temperature of electrons in the hot plasma are 0.035 cm^{-3} and 3.51×10^6 K (Ott et al. 2005), respectively, the expected dust temperature ranges from 15 to 30 K due to collisional heating. Thus, it is likely that the collisional heating process significantly contributes to dust heating especially in the northern IR-halo region.

5 CONCLUSIONS

AKARI and Herschel images at wavelengths from 7 μm to 500 μm show a diffuse IR emission extending from the galactic disk into the halo region. The most prominent filamentary structure seen in the diffuse IR emission is spatially in good agreement with the western arm seen in the $\text{H}\alpha$. The spatial distribution of the F_{350}/F_{500} map shows high values in regions around the SSCs and towards the western arm, which are not found in the F_{250}/F_{350} map. The color-color diagram of F_{250}/F_{350} – F_{350}/F_{500} indicates enhanced β_c in those regions. From a spectral decomposition analysis on the pixel-by-pixel basis, we obtained β_c , T_c , and T_w maps; the β_c map shows values ranging from ~ 1 to ~ 2 over the whole galaxy. In particular, high β_c values of ~ 2 are observed in the regions indicated by the color-color diagram. As for the T_c and T_w maps, those show high temperatures on the northern side than on the southern side in the IR-halo region.

Since the average cold dust temperature in NGC 1569 is ~ 30 K, $\beta_c < 2.0$ in the far-IR and sub-mm region theoretically suggests thermal emission from amorphous grains, while $\beta_c = 2.0$ suggests that from crystal grains. Given that the enhanced β_c regions are spatially confined by the HI ridge that is considered to be a birthplace of the SSCs, the spatial coincidences may indicate that dust grains around the SSCs are crystalline ones injected by massive stars originating from starburst activities as have been found in ultra-luminous infrared galaxies and that those grains are blown away along the HI ridge and thus the western arm.

The observed asymmetric temperature distribution

with respect to the disk cannot be explained solely by radiative dust heating by stars distributed over the disk. Given that the presence of the hot plasma in the IR-halo region, it is likely that the collisional heating process significantly contributes to dust heating especially in the northern IR-halo region.

ACKNOWLEDGMENTS

This research is based on observations with AKARI, a JAXA project with the participation of ESA.

PACS has been developed by a consortium of institutes led by MPE (Germany) and including UVIE (Austria); KU Leuven, CSL, IMEC (Belgium); CEA, LAM (France); MPIA (Germany); INAF-IFSI/OAA/OAP/OAT, LENS, SISSA (Italy); IAC (Spain). This development has been supported by the funding agencies BMVIT (Austria), ESA-PRODEX (Belgium), CEA/CNES (France), DLR (Germany), ASI/INAF (Italy), and CICYT/MCYT (Spain).

SPIRE has been developed by a consortium of institutes led by Cardiff University (UK) and including Univ. Lethbridge (Canada); NAOC (China); CEA, LAM (France); IFSI, Univ. Padua (Italy); IAC (Spain); Stockholm Observatory (Sweden); Imperial College London, RAL, UCL-MSSL, UKATC, Univ. Sussex (UK); and Caltech, JPL, NHSC, Univ. Colorado (USA). This development has been supported by national funding agencies: CSA (Canada); NAOC (China); CEA, CNES, CNRS (France); ASI (Italy); MCINN (Spain); SNSB (Sweden); STFC, UKSA (UK); and NASA (USA).

This work made use of THINGS, 'The HI nearby Galaxy Survey' (Walter et al. 2008).

REFERENCES

- Aguirre A., Schaye J., Quataert E., 2001, *ApJ*, **561**, 550
 Angeretti L., Tosi M., Greggio L., Sabbi E., Aloisi A., Leitherer C., 2005, *AJ*, **129**, 2203
 Aniano G., Draine B. T., Gordon K. D., Sandstrom K., 2011, *PASP*, **123**, 1218
 Arimatsu K., et al., 2011, *PASP*, **123**, 981
 Arp H., Sandage A., 1985, *AJ*, **90**, 1163
 Bendo G. J., et al., 2012, *MNRAS*, **419**, 1833
 Bendo G. J., et al., 2015, *MNRAS*, **448**, 135
 Boselli A., et al., 2012, *A&A*, **540**, A54
 Casey C. M., 2012, *MNRAS*, **425**, 3094
 Cazzoli S., Arribas S., Colina L., Piqueras-López J., Bellocchi E., Emonts B., Maiolino R., 2014, *A&A*, **569**, A14
 Draine B. T., Li A., 2007, *ApJ*, **657**, 810
 Dwek E., 1987, *ApJ*, **322**, 812
 Erb D. K., Quider A. M., Henry A. L., Martin C. L., 2012, *ApJ*, **759**, 26
 Galliano F., Madden S. C., Jones A. P., Wilson C. D., Bernard J.-P., Le Peintre F., 2003, *A&A*, **407**, 159
 Griffin M. J., et al., 2010, *A&A*, **518**, L3
 Heckman T. M., Dahlem M., Lehnert M. D., Fabbiano G., Gilmore D., Waller W. H., 1995, *ApJ*, **448**, 98
 Hodge P. W., 1974, *ApJ*, **191**, L21
 Hunter D. A., Elmegreen B. G., 2004, *AJ*, **128**, 2170
 Hunter D. A., Hawley W. N., Gallagher III J. S., 1993, *AJ*, **106**, 1797
 Hunter D. A., O'Connell R. W., Gallagher J. S., Smecker-Hane T. A., 2000, *AJ*, **120**, 2383

- Israel F. P., van Driel W., 1990, *A&A*, **236**, 323
- Johnson M., 2013, *AJ*, **145**, 146
- Johnson M., Hunter D. A., Oh S.-H., Zhang H.-X., Elmegreen B., Brinks E., Tollerud E., Herrmann K., 2012, *AJ*, **144**, 152
- Kaneda H., Koo B. C., Onaka T., Takahashi H., 2009a, *Advances in Space Research*, **44**, 1038
- Kaneda H., Onaka T., Suzuki T., Takahashi H., Yamagishi M., 2009b, in T. Onaka, G. J. White, T. Nakagawa, & I. Yamamura ed., *Astronomical Society of the Pacific Conference Series Vol. 418, AKARI, a Light to Illuminate the Misty Universe*. pp 197–+
- Kaneda H., et al., 2010, *A&A*, **514**, A14
- Kemper F., Markwick A. J., Woods P. M., 2011, *MNRAS*, **413**, 1192
- Li A., Draine B. T., 2001, *ApJ*, **554**, 778
- Lianou S., Barmby P., Rémy-Ruyer A., Madden S. C., Galliano F., Lebouteiller V., 2014, *MNRAS*, **445**, 1003
- Madden S. C., et al., 2013, *PASP*, **125**, 600
- Martin C. L., 1998, *ApJ*, **506**, 222
- Martin C. L., Kobulnicky H. A., Heckman T. M., 2002, *ApJ*, **574**, 663
- Meny C., Gromov V., Boudet N., Bernard J.-P., Paradis D., Nayral C., 2007, *A&A*, **468**, 171
- Micelotta E. R., Jones A. P., Tielens A. G. G. M., 2010, *A&A*, **510**, A36+
- Montier L. A., Giard M., 2004, *A&A*, **417**, 401
- Mühle S., Klein U., Wilcots E. M., Hüttmeister S., 2005, *AJ*, **130**, 524
- Murakami H., et al., 2007, *PASJ*, **59**, 369
- Onaka T., et al., 2007, *PASJ*, **59**, 401
- Onaka T., Matsumoto H., Sakon I., Kaneda H., 2010, *A&A*, **514**, A15
- Ott J., Walter F., Brinks E., 2005, *MNRAS*, 358
- Paradis D., Bernard J.-P., Mény C., Gromov V., 2011, *A&A*, **534**, A118
- Pilbratt G. L., et al., 2010, *A&A*, **518**, L1
- Poglitsch A., et al., 2010, *A&A*, **518**, L2
- Rémy-Ruyer A., et al., 2013, *A&A*, **557**, A95
- Rémy-Ruyer A., et al., 2015, *A&A*, **582**, A121
- Roussel H., et al., 2010, *A&A*, **518**, L66
- Spoon H. W. W., et al., 2006, *ApJ*, **638**, 759
- Suzuki T., Kaneda H., Onaka T., Nakagawa T., Shibai H., 2010, *A&A*, **521**, A48+
- Tabatabaei F. S., et al., 2014, *A&A*, **561**, A95
- Walter F., Brinks E., de Blok W. J. G., Bigiel F., Kennicutt Jr. R. C., Thornley M. D., Leroy A., 2008, *AJ*, **136**, 2563
- Westmoquette M. S., Smith L. J., Gallagher J. S., 2008, *MNRAS*, **383**, 864
- Yoshida M., Kawabata K., Ohya Y., 2011, *PASJ*, **63**, 493
- Zu Y., Weinberg D. H., Davé R., Fardal M., Katz N., Kereš D., Oppenheimer B. D., 2011, *MNRAS*, **412**, 1059

This paper has been typeset from a $\text{\TeX}/\text{\LaTeX}$ file prepared by the author.